Non-Spectroscopic Composition Measurements of $SrTiO_3$-$La_{0.7}Sr_{0.3}MnO_3$ Multilayers using Scanning Convergent Beam Electron Diffraction

Colin Ophus,[1,*] Peter Ercius,[1] Mark Huijben,[2] and Jim Ciston[1]

[1]*National Center for Electron Microscopy, Molecular Foundry, Lawrence Berkeley National Laboratory, CA, USA*

[2]*Faculty of Science and Technology, University of Twente, The Netherlands*

(Dated: January 17, 2017)

Abstract

The local atomic structure of a crystalline sample aligned along a zone axis can be probed with a focused electron probe, which produces a convergent beam electron diffraction pattern. The introduction of high speed direct electron detectors has allowed for experiments that can record a full diffraction pattern image at thousands of probe positions on a sample. By incoherently summing these patterns over crystalline unit cells, we demonstrate that in addition to crystal structure and thickness we can also estimate the local composition of a perovskite superlattice sample. This is achieved by matching the summed patterns to a library of simulated diffraction patterns. This technique allows for atomic-scale chemical measurements without requiring a spectrometer or hardware aberration correction.

* cophus@gmail.com

Traditional scanning transmission electron microscopy (STEM) detectors are monolithic and integrate a subset of the transmitted electron beam signal scattered from each electron probe position. These convergent beam electron diffraction patterns (CBED) are extremely rich in information, containing localized information on sample structure [1], composition [2], phonon spectra [3], three-dimensional defect crystallography [4], local lattice strains [5] and more. Many new imaging modes become possible if the full CBED pattern is recorded at many probe positions with millisecond dwell times [6–9]. Such a four-dimensional dataset is comprised of a 2D CBED pattern at each point in a 2D grid of STEM probe positions, hence the name 4D-STEM.

Local structural distortions are responsible for a wide variety of properties in perovskite films and strain-engineered multilayers [10–19]. Atomic resolution aberration corrected STEM can be used to precisely measure few-picometer shifts in the positions of atomic columns, which has been shown to directly measure polarization [20]. However, as in the case of stain measurement outlined above this is highly limited by the sample quality, precision of zone axis tilting, and instrument alignment. Position averaged convergent beam electron diffraction (PACBED) described by LeBeau et al. [21] has been shown to quantitatively measure ferroelectric polarization, octahedral tilts and overall sample tilt at a fixed nanoscale location [22–24], and is insensitive to residual aberrations in the electron microscope. By comparing the experimental data to a library of previously computed PACBED patterns it is possible to determine both the magnitude and direction of ferroelectric polarization [23]. PACBED has also revealed the octahedral distortions responsible for the extreme carrier densities in $SrTiO_3/GdTiO_3$ quantum wells [25].

Conventionally, PACBED measurements are acquired by collecting a diffraction pattern on a typical CCD with ≈1 second acquisition time while the STEM probe is continuously rastered over a predefined area of the sample (approximately 1 nm^2). Using 4D-STEM, every individual CBED pattern is recorded with ≈1 millisecond acquisition time second during the course of a STEM scan (<0.01 nm^2 sampling), and PACBED images can be computed during data post-processing. This confers a significant advantage in that many PACBED patterns can be assembled from precisely defined sample regions of arbitrary shape with unit cell resolution. This is critically important for the experimental case of multilayer films with sharp interfaces where it is desirable to measure polarization and distortion for every unit cell near and across the interface with minimal crosstalk from sample drift or misregistration

of a conventionally predefined integrated region.

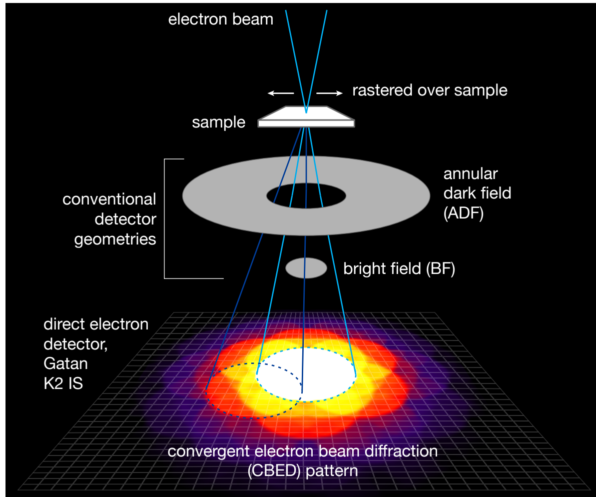

FIG. 1. Experimental STEM setup showing the conventional ADF and BF detectors, which record a single value per probe position. Below is the camera used in this study instead of a BF detector, a high-speed direct electron detector which records a full CBED pattern for each probe position.

The experimental geometry is shown schematically in Fig. 1. In this study, we used a Gatan K2 IS direct electron detection camera installed on an uncorrected FEI Titan-class transmission electron microscope to record 4D-STEM probe diffraction patterns on a variety of samples at 800 frames per second. The annular dark field (ADF) signal was recorded simultaneously using a monolithic Fischione detector. All data processing was performed using the Gatan Digital Micrograph software package and custom analysis code written in MATLAB. Specimens were prepared for electron microscopy by affixing a sacrificial Si crystal in a face-to-face geometry before cross-sectional slicing with a diamond saw. Mechanical polishing in a wedge geometry was used to thin the sample to electron transparency. Final thinning and removal of residual surface damage was accomplished by Ar+ ion milling in a Gatan Precision Ion Polishing System under 5 degrees and 2 keV with liquid nitrogen cooling.

Using 4D-STEM, we have produced PACBED maps of a $SrTiO_3/(La_{0.7}Sr_{0.3})MnO_3$ multilayer magnetic tunnel junction [26–28] at a spatial resolution of one unit cell (0.4 nm^2), centered on the A sites (Sr/La columns). The multilayer sample consisted of 120 bilayers, each consisting of 4 unit cells of $(La_{0.7}Sr_{0.3})MnO_3$ (1.551 nm) and 4 unit cells of $SrTiO_3$ (1.561 nm), and was fabricated using the pulsed laser deposition (PLD) technique (see de-

tails in [27, 28]). The transport and magnetic properties of the $SrTiO_3/(La_{0.7}Sr_{0.3})MnO_3$ multilayer have been reported in a previous study [28]. A 4D-STEM dataset was acquired at 16,384 probe positions with a sampling interval of 0.025 nm for a total data size of 300 Gigabytes. Using the simultaneously acquired HAADF data, a reference lattice was refined to the perovskite structure, which was then used to parse the individual CBED frames into single unit cell bins. Figs. 2a and b shows conventional HAADF STEM images and PACBED maps at unit cell resolution reconstructed from this data. This data was collected on a conventional FEI Titan microscope without aberration correction at 200 keV with a 10.5 mrad probe convergence semiangle. STEM electron energy loss spectroscopy (EELS) data was collected on a probe-corrected Titan at 300 keV with a 17 mrad convergence semiangle and 59 mrad collection semiangle. Line scans were collected with a 0.1 nm step size and deconvolved with the 0.9 eV FWHM zero loss peak prior to quantification. Power law background and Hartree-Slater cross sections were used for quantification. A comparable, but not identical, region of the sample was used for both the PACBED and STEM-EELS experiments to minimize any effects of sample thickness and variance in interfacial sharpness as a function of sample growth layer number.

In order to demonstrate the viability of a library approach to mapping of local properties through quantitative PACBED analysis, we first attempted to determine the local composition of each unit cell using only diffraction information. We matched the experimental patterns to PACBED images simulated with the multislice method [29] to determine parameters such as sample thickness and composition. A library of PACBED patterns was calculated assuming ideal mixing of $SrTiO_3$ and $(La_{0.7}Sr_{0.3})MnO_3$ in 5% compositional increments from pure $SrTiO_3$ to pure $(La_{0.7}Sr_{0.3})MnO_3$. The site occupancies were always set to either one species or the other, randomized over the entire atomic column and averaged over many probe locations, which also accounted for thermal vibration by including many frozen phonon configurations [29]. The simulated thickness was varied from 0-40 nm in increments of one unit cell (0.3095 nm). A subset of the simulated PACBED images are plotted in Fig. 2c. The best match between the experimental and simulated PACBED images was assumed to be the one with the lowest mean absolute difference between the images.

From this library of simulated diffraction patterns, the best overall fit for thickness across the first dataset in Figs. 3a-d was found to be 12.5 ± 0.3 nm, which was then fixed for all unit cells in the field of view. The thickness error was estimated from the standard

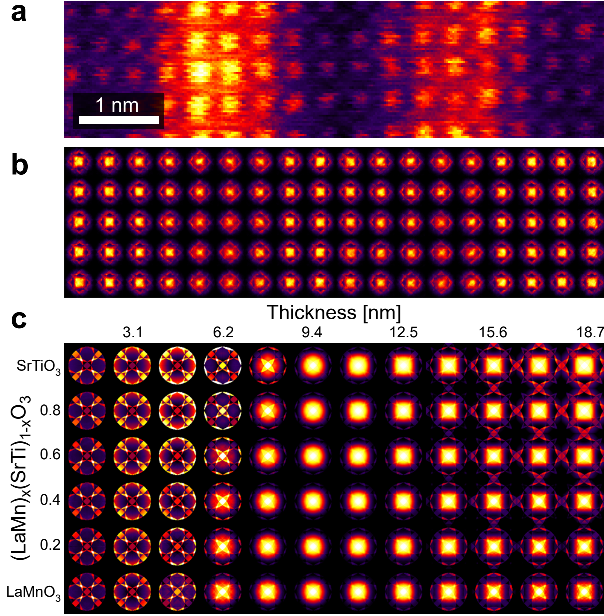

FIG. 2. (a) Atomic resolution HAADF STEM image and (b) PACBED map at unit cell resolution of 0.4 nm for a $SrTiO_3/(La_{0.7}Sr_{0.3})MnO_3$ multilayer heterojunction acquired with the high speed direct electron detector. (c) Multislice simulations of CBED patterns for $(LaMn)_x(SrTi)_{1-x}O_3$. Note that contrast is scaled to show full range of intensities in the center disk.

deviation of all unit cell fits. The low thickness error is due to the strong dependence of the PACBED contrast on thickness. A least squares fit was then performed for every experimental PACBED pattern to determine the local composition of each projected unit cell. This composition data is plotted in Figs. 3c and d. The alternating composition of the two superlattice layers is clearly visible, including an asymmetry between the two interface types.

A second PACBED dataset from a thinner region of the sample is shown in Figs. 3e-h. The best-fit thickness of these cells was found to be 7.5 ± 0.5 nm. The composition range between the two superlattice layers in this dataset is quite similar to the previous dataset, though with larger variances perpendicular to the growth direction (shown as larger error bars in the plot). This suggests that the primary source of error is the extra diffraction signal generated by amorphous regions on both sample surfaces. Because this region of the sample is thinner, the signal of the bulk here is relatively smaller with respect to the surface signal, which is expected to be a similar magnitude in both datasets. Another possibility is that the PACBED signal varies more slowly with thickness and composition for small

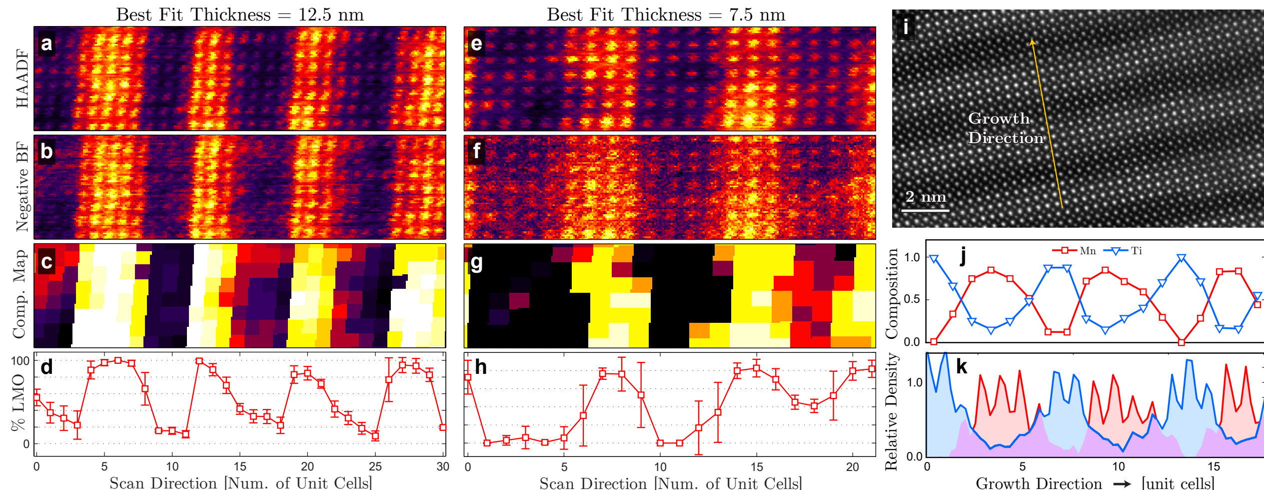

FIG. 3. Composition measurements of $(\mathrm{LaMn})_x(\mathrm{SrTi})_{1-x}\mathrm{O}_3$ with PACBED and STEM-EELS. (a,e) HAADF image, (b,f) negative virtual BF image, (c,g) unit cell composition maps from best-fit matches to the simulations, and (d,h) averaged composition parallel to the film growth direction for two different sample regions. Error bars show estimated error from the standard deviation along the vertical direction, perpendicular to growth direction. (i) Aberration-corrected HAADF image with the position of an EELS line scan, plotted in (j) and (k).

thickness values.

These PACBED-fit compositions were compared with a conventional STEM-EELS line scan to determine the local ratio of Ti and Mn atoms for each unit cell, shown in Figs. 3i-k. While the absolute composition is slightly mismatched on the order of 10% between PACBED and EELS, the asymmetric composition gradient is faithfully reproduced, demonstrating the validity of extracting local structural information with unit cell resolution from quantitative fitting of 4D-STEM data to PACBED simulations. A more direct analysis of the relative error of the two methods will require future experimental measurements at the exact same sample region.

In summary, we have used a direct electron detector to record an experimental 4D-STEM dataset of a $(\mathrm{LaMn})_x(\mathrm{SrTi})_{1-x}\mathrm{O}_3$ perovskite superlattice sample. This dataset consisted of a full CBED pattern at each STEM probe position, which was integrated over each unit cell to produce a PACBED pattern. By calculating a library of PACBED images with multislice simulations, we have calculated best-fit compositions and thicknesses for the superlattice samples. The measured compositions were verified using an aberration-

corrected STEM-EELS line scan. Our results show that 4D-STEM PACBED experiments can measure chemical composition with high accuracy, without requiring a spectrometer or aberration-corrected STEM probes. Furthermore, the elastic scattering cross section is much higher than the inelastic cross section for core loss events or x-ray generation, which opens the possibility for measuring composition at greater dose efficiency than conventional chemical mapping techniques.

The authors wish to thank Cory Czarnik, Karen Bustillo, Marissa Libbee, and Michael Sarahan for their help with the experiments presented here. Work at the Molecular Foundry was supported by the Office of Science, Office of Basic Energy Sciences, of the U. S. Department of Energy under Contract No. DE-AC02-05CH11231. JC acknowledges additional support from the U. S. Department of Energy Early Career Research Program.

---

[1] J. Spence, Acta Crystallographica Section A: Foundations of Crystallography **49**, 231 (1993).

[2] C. Humphreys, D. Eaglesham, D. Maher, and H. Fraser, Ultramicroscopy **26**, 13 (1988).

[3] D. A. Muller, B. Edwards, E. J. Kirkland, and J. Silcox, Ultramicroscopy **86**, 371 (2001).

[4] R. t. Carpenter and J. Spence, Acta Crystallographica Section A: Crystal Physics, Diffraction, Theoretical and General Crystallography **38**, 55 (1982).

[5] V. Ozdol, C. Gammer, X. Jin, P. Ercius, C. Ophus, J. Ciston, and A. Minor, Applied Physics Letters **106**, 253107 (2015).

[6] N. Shibata, S. D. Findlay, Y. Kohno, H. Sawada, Y. Kondo, and Y. Ikuhara, Nature Physics **8**, 611 (2012).

[7] C. Ophus, J. Ciston, J. Pierce, T. R. Harvey, J. Chess, B. J. McMorran, C. Czarnik, H. H. Rose, and P. Ercius, Nature communications **7** (2016).

[8] H. Yang, R. Rutte, L. Jones, M. Simson, R. Sagawa, H. Ryll, M. Huth, T. Pennycook, M. Green, H. Soltau, *et al.*, Nature Communications **7** (2016).

[9] H. Yang, P. Ercius, P. D. Nellist, and C. Ophus, Ultramicroscopy **171**, 117 (2016).

[10] S. Bhattacharjee, E. Bousquet, and P. Ghosez, Physical Review Letters **102** (2009), Artn 117602 Doi 10.1103/Physrevlett.102.117602.

[11] G. Catalan, A. Lubk, A. H. G. Vlooswijk, E. Snoeck, C. Magen, A. Janssens, G. Rispens, G. Rijnders, D. H. A. Blank, and B. Noheda, Nat Mater **10**, 963 (2011).

[12] K. J. Choi, M. Biegalski, Y. L. Li, A. Sharan, J. Schubert, R. Uecker, P. Reiche, Y. B. Chen, X. Q. Pan, V. Gopalan, L.-Q. Chen, D. G. Schlom, and C. B. Eom, Science **306**, 1005 (2004).

[13] A. J. Grutter, H. Yang, B. J. Kirby, M. R. Fitzsimmons, J. A. Aguiar, N. D. Browning, C. A. Jenkins, E. Arenholz, V. V. Mehta, U. S. Alaan, and Y. Suzuki, Physical Review Letters **111** (2013), 10.1103/Physrevlett.111.087202.

[14] J. M. Rondinelli, S. J. May, and J. W. Freeland, MRS Bulletin **37**, 261 (2012).

[15] M. B. Salamon and M. Jaime, Reviews of Modern Physics **73**, 583 (2001).

[16] M. Stengel, D. Vanderbilt, and N. A. Spaldin, Nature Materials **8**, 392 (2009).

[17] K. S. Takahashi, M. Kawasaki, and Y. Tokura, Applied Physics Letters **79**, 1324 (2001).

[18] H. Yamada, M. Marinova, P. Altuntas, A. Crassous, L. Begon-Lours, S. Fusil, E. Jacquet, V. Garcia, K. Bouzehouane, A. Gloter, J. E. Villegas, A. Barthelemy, and M. Bibes, Scientific Reports **3** (2013), 10.1038/Srep02834.

[19] M. Danaie, D. Kepaptsoglou, Q. M. Ramasse, C. Ophus, K. R. Whittle, S. M. Lawson, S. Pedrazzini, N. P. Young, P. A. Bagot, and P. D. Edmondson, Inorganic Chemistry (2016).

[20] C. T. Nelson, B. Winchester, Y. Zhang, S.-J. Kim, A. Melville, C. Adamo, C. M. Folkman, S.-H. Baek, C.-B. Eom, D. G. Schlom, L.-Q. Chen, and X. Pan, Nano Letters **11**, 828 (2011).

[21] J. M. LeBeau, S. D. Findlay, L. J. Allen, and S. Stemmer, Ultramicroscopy **110**, 118 (2010).

[22] J. M. LeBeau, A. J. D'Alfonso, N. J. Wright, L. J. Allen, and S. Stemmer, Applied Physics Letters **98**, 3 (2011).

[23] J. Hwang, J. Y. Zhang, J. Son, and S. Stemmer, Applied Physics Letters **100** (2012), 10.1063/1.4714734.

[24] H. Brown, R. Ishikawa, G. Sánchez-Santolino, N. Lugg, Y. Ikuhara, L. Allen, and N. Shibata, Ultramicroscopy (2016).

[25] J. Y. Zhang, J. Hwang, S. Raghavan, and S. Stemmer, Physical Review Letters **110** (2013), 10.1103/Physrevlett.110.256401.

[26] C. Aruta, C. Adamo, A. Galdi, P. Orgiani, V. Bisogni, N. B. Brookes, J. C. Cezar, P. Thakur, C. A. Perroni, G. De Filippis, V. Cataudella, D. G. Schlom, L. Maritato, and G. Ghiringhelli, Physical Review B **80** (2009), 10.1103/Physrevb.80.140405.

[27] A. X. Gray, C. Papp, B. Balke, S. H. Yang, M. Huijben, E. Rotenberg, A. Bostwick, S. Ueda, Y. Yamashita, K. Kobayashi, E. M. Gullikson, J. B. Kortright, F. M. F. de Groot, G. Rijnders, D. H. A. Blank, R. Ramesh, and C. S. Fadley, Physical Review B **82** (2010), 10.1103/Phys-

RevB.82.205116.

[28] A. X. Gray, J. Minar, L. Plucinski, M. Huijben, A. Bostwick, E. Rotenberg, S. H. Yang, J. Braun, A. Winkelmann, G. Conti, D. Eiteneer, A. Rattanachata, A. A. Greer, J. Ciston, C. Ophus, G. Rijnders, D. H. A. Blank, D. Doennig, R. Pentcheva, J. B. Kortright, C. M. Schneider, H. Ebert, and C. S. Fadley, Epl **104** (2013), 10.1209/0295-5075/104/17004.

[29] E. J. Kirkland, *Advanced computing in electron microscopy* (Springer Science & Business Media, 2010).